Chem. Res. Chinese Universities, 2020, 36(6), 1024—1031 doi: 10.1007/s40242-020-0067-5

Article

Synthesis of Holey Graphitic Carbon Nitride with Highly Enhanced Photocatalytic Reduction Activity *via* Melamine-cyanuric Acid Precursor Route

QI Yinhong, XU Jixiang*, WANG Chao, ZHAN Tianrong and WANG Lei*

Key Laboratory of Eco-chemical Engineering, Ministry of Education, State Laboratory of Inorganic Synthesis and Applied Chemistry, College of Chemistry and Molecular Engineering, Qingdao University of Science and Technology, Qingdao 266042, P. R. China

Abstract In this work, holey graphitic carbon nitride(HCN) was prepared by one-step thermal polymerization of hydrothermal product of melamine and then loaded with Ni/MoO_2(NiMo) cocatalyst obtained by $NaBH_4$ reduction process. The obtained material was used for photocatalytic production of H_2 from water reduction and H_2O_2 production from O_2 reduction. The best photocatalyst(1% NiMo/HCN) exhibited a H_2 evolution rate of 8.08 μmol/h while no H_2 was detected over 1% NiMo-modifed bulk g-C_3N_4(BCN) under visible light illumination. Moreover, this rate is 1.7 times higher than that of 1% Pt-modified HCN. The 1% NiMo/HCN catalyst also exhibited the highest H_2O_2 production activity with a value of 6.13 μmol/h. Such enhancement was ascribed to the efficient charge carrier separation and migration, which were promoted by the large specific surface area and pore volume of HCN and the synergy between MoO_2 and Ni. The proposed method to obtain HCN is expected to open up new ways in development of highly-active HCN-based photocatalysts for photocatalytic reduction reactions.

Keywords Holey g-C_3N_4; Ni/MoO_2 nanoparticle; Photocatalysis; H_2 evolution; H_2O_2 production

1 Introduction

Solar light-driven photocatalytic water reduction to generate hydrogen(H_2) and photocatalytic O_2 reduction to produce H_2O_2 are considered as promising strategies to replace traditional fossil fuels for alleviating the energy crisis and environmental pollution. The development of effective photocatalysts, with high capacity to absorb visible light and high charge separation efficiency for efficient H_2 and H_2O_2 production, is the key to successfully perform such process[1,2]. At present, g-C_3N_4(CN) has attracted much attention due to its low cost and narrow bandgap(about 2.6 eV)[3,4]. However, the intrinsic photocatalytic activity of CN obtained by direct annealing of N-rich molecules is not high due to the poor light absorption, small specific surface area(SSA), and low charge separation efficiency. Thus, to improve the photocatalytic performance of CN, optimizing the charge separation and bandgap structures by different approaches, such as heteroatoms doping, cocatalyst decoration, and coupling CN with other semiconductors, was reported already[5—9]. The modification of CN morphology and textural properties(particularly, the specific surface area) are alternative strategies to improve the photocatalytic properties of CN[7,10—12]. For instance, it was shown that generating holes in CN can greatly improve the photocatalytic performance compared to bulk CN(BCN), because these in-plane holes can not only enhance the mass and charge transport, but also effectively prevent the aggregation of CN nanosheets by reducing their contact sites[13—24].

Several previous works found that holey or porous CN(HCN) can be prepared by NH_3-mediated polymerization process[15,25—27] or thermally treating BCN under an NH_3 atmosphere[28]. Zhou *et al*.[29] prepared HCN with more uncondensed amino groups by heating melamine under self-producing atmosphere. Despite many endeavors have been made to fabricate HCN[13—30], developing a simple approach to synthesize HCN nanosheets with large surface area is still needed. Recently, Zhang *et al*.[31] synthesized CN microtubes by thermal polymerization hydrothermal product of melamine(melamine-cyanuric acid, MCA). It was found that gases(NH_3, CO_2, etc.) can be released during annealing of MCA[19,32,33]. In line with these results, we propose herein the preparation of HCN nanosheets by thermal polymerization of hydrothermal product of melamine(Scheme 1) to explore the tubular morphology of MCA, aiming to prevent the aggregation of CN nanosheets. In addition, the self-production of NH_3 and CO_2 acted as etching agents to form holes on the surface of CN. Then, the HCN was decorated with Ni/MoO_2(NiMo) nanoparticles(NPs) *via* physical grinding to obtain HCN/NiMo photocatalyst. Compared to NiMo-modified BCN obtained by direct annealing of melamine, the HCN/NiMo exhibited significantly

*Corresponding authors. Email: inorchemwl@126.com; xujix47@163.com

Received March 20, 2020; accepted April 20, 2020.

Supported by the National Natural Science Foundation of China(Nos.21571112, 51772162) and the Taishan Scholar Program of Advantage and Characteristic Discipline Team of Eco Chemical Process and Technology, China.

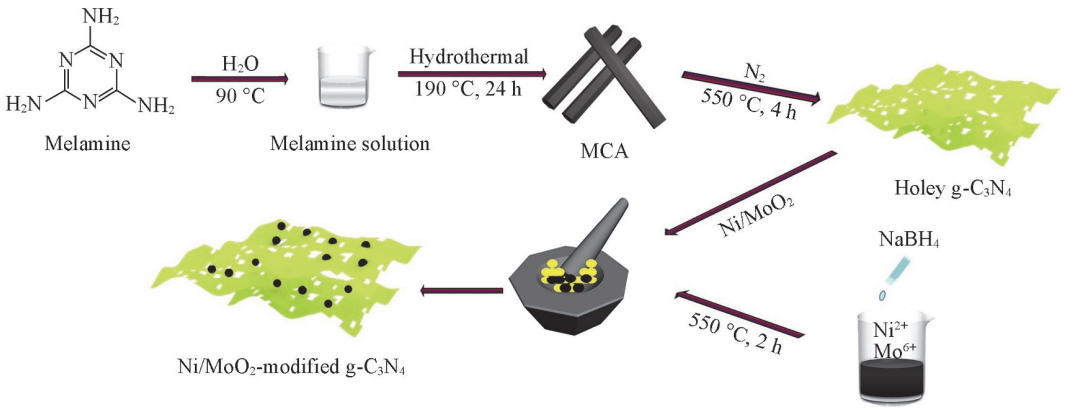

Scheme 1 Schematic representation of the synthesis of NiMo/HCN photocatalyst

improved photocatalytic H_2 and H_2O_2 production performance.

2 Experimental

2.1 Preparation of HCN and NiMo/HCN

MCA was synthesized *via* a hydrothermal method according to Zhang's work[31] excepting the hydrothermal temperature, which was 190 °C(see the Electronic Supplementary Material of this paper). For the preparation of HCN, certain amount(0.2, 0.3 and 0.5 g) of MCA precursor was first ground in a mortar for 30 min and then calcined at 550 °C for 4 h in a muffle furnace, at a ramp rate of 5 °C/min under N_2 atmosphere with different flow rates(20, 30 and 50 mL/min). BCN was prepared by calcination of pure melamine(3 g) at 550 °C for 4 h and used as reference.

NiMo NPs were synthesized *via* a $NaBH_4$ reduction method. Firstly, 0.0375 mmol of $NiCl_2{\cdot}6H_2O$, 0.0125 mmol of Na_2MoO_4, and 48 mg of PVP were mixed with 4 mL of distilled water. After the mixture was dissolved, 1 mL of $NaBH_4$ solution(0.52 mol/L) was added and stirred at room temperature until no bubbles were generated. The resulted black product was centrifuged and washed several times with deionized water and then dried at 60 °C under vacuum. Finally, the obtained black solid was heated at 550 °C for 2 h with a heating rate of 20 °C/min under N_2 atmosphere.

For the preparation of NiMo/HCN photocatalyst, 100 mg of prepared HCN and various amounts of the synthesized NiMo NPs were mixed and ground in a mortar for 10 min. The obtained samples were labeled as *m*NiMo/HCN, where *m*(0.5%, 1%, 2%, and 3%) represents the mass percent of NiMo in the final solid. Reference samples, *i.e.*, 1% NiMo/BCN, 1% Pt/HCN, and 1% Pt/BCN, were obtained by the same method used to prepare NiMo/HCN but using BCN as support and Pt as cocatalyst.

2.2 Characterization

Powder X-ray diffraction(XRD) data were collected on a Rigaku D-MAX 2500/PC diffractometer equipped with a Cu *Kα* radiation source. X-Ray photoelectron spectra(XPS) were recorded on an X-ray photoelectron spectrometer(Thermo Scientific, *Kα*) equipped with a monochromatic Al *Kα* X-ray source(*hv*=1486.6 eV). UV-visible diffuse reflectance(UV-Vis DR) spectra were recorded on a Lambda 750 UV/VIS/NIR spectrometer. The morphology of each as-made sample was investigated by using a scanning electron microscopy(SEM) instrument. High-angle annular dark field scanning TEM (HAADF-STEM) images coupled with energy dispersive spectroscopy (EDS) elemental mapping were recorded on a Bruker Super-X EDS. A fluor-spectrophotometer(F-4500 FL) was used to record photoluminescence(PL) spectra. The electron spin response(ESR) signal of $\cdot O^{2-}$ was obtained with a JEOL JES-FA200 spectrometer under visible light irradiation($\lambda \geqslant 420$ nm). DMPO(5,5-dimethyl-l-pyrrolidine *N*-oxide) was used as the spin trap.

2.3 Photocatalytic Production of H_2 and H_2O_2

The photocatalytic H_2 evolution was obtained in a quartz flask equipped with a flat optical entry window. The photocatalysts(10 mg) were dispersed into 100 mL of 15% triethanolamine(TEOA) aqueous solution, as sacrificial agent. Before light irradiation, the system was deaerated by bubbling N_2 into the solution for 30 min. A 300-W Xe lamp with cutoff filter ($\lambda \geqslant 420$ nm) was used as the visible-light source. The amount of H_2 evolved was determined using an online gas chromatography system(GC-7920). The apparent quantum efficiency (AQE, %) was measured under the same conditions of the photocatalytic reaction, an irradiation time of 60 min, and cal- culated using the following equation:

$$\mathrm{AQE}(\%) = \frac{2 \times \text{The number of evolved hydrogen molecules}}{\text{The number of incident photons}} \times 100\%$$

For photocatalytic H_2O_2 production, 10 mg of the photocatalyst was dispersed in 50 mL of 5% ethanol aqueous solution or ultrapure water. Then, O_2 was continually bubbled to achieve saturation adsorption. Afterwards, the suspension was irradiated with simulated sunlight(filter: AM1.5). At regular intervals of time, 3 mL of the suspension was collected. The produced H_2O_2 concentration was determined by iodometry[34]. The H_2O_2 decomposition behavior was studied by dispersing 10 mg of photocatalyst in 50 mL of 1 mmol/L H_2O_2 solution and irradiating for 3 h under continuous stirring. To evaluate the recyclability of the photocatalyst, the sample was collected by centrifugation, washed three times with deionized water, and

dried before use in the next cycle experiments.

3 Results and Discussion

3.1 Photocatalyst Characterization

As shown in Fig.1(A), the MCA precursor displays a hexagonal-like morphology. The XRD pattern is different from that of melamine(Fig.S1, see the Electronic Supplementary Material of this paper), and similar to that reported previously for MCA[31]. The shift of the band vibration of triazine ring in melamine from 814 cm^{-1} to 771 cm^{-1} in the corresponding FTIR spectrum(Fig.S2, see the Electronic Supplementary Material of this paper) also confirms the formation of the MCA complex between melamine and cyanuric acid by hydrogen bonds[35,36]. After annealing 0.3 g of MCA at 550 °C for 4 h under N_2 with a flow rate of 30 mL/min, the transition from hexagonal rod to holey sheets has occurred, as shown in Fig.1(B). The FTIR spectrum of this sample is similar with that of BCN(Fig.S2, see the Electronic Supplementary Material of this paper), demonstrating their similar chemical structures. Hence, the bands at 1200—1650 cm^{-1} correspond to the typical stretching modes of CN heterocycles while the band at 813 cm^{-1} is assigned to the out-of-plane bending of the s-triazine units[31,35,36]. Moreover, the XRD pattern of the annealed MCA displays two distinct diffraction peaks at *ca*. 13.1° and *ca*. 27.5°(Fig.2 and Fig.S3, see the Electronic Supplementary Material of this paper), which can be assigned to (100) and (002) crystal planes of graphite-like CN. Yet, these two diffraction peaks are less intense compared to those of BCN, evidence of a lower crystallinity(Fig.S3). The results of SEM, FTIR and XRD demonstrate the transformation of the MCA rods into HCN.

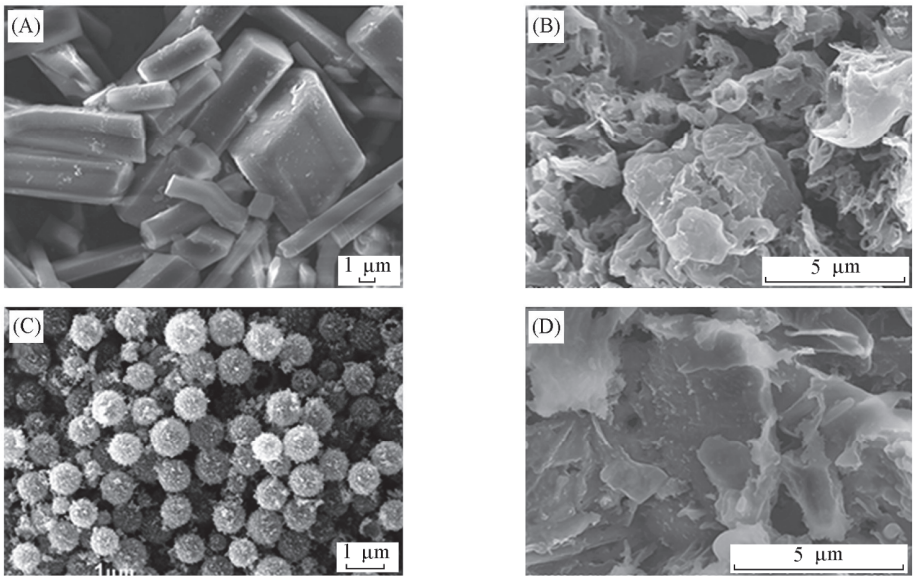

Fig.1 SEM images of the prepared MCA(A), HCN(B), NiMo NPs(C) and 1% NiMo/HCN composite(D)

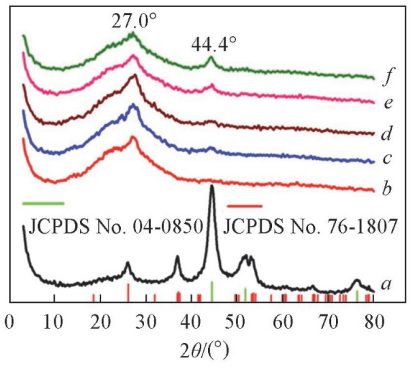

Fig.2 XRD patterns of NiMo(*a*), HCN(*b*) and NiMo/HCN with 0.5%(*c*), 1%(*d*), 2%(*e*) and 3%(*f*) NiMo

To shed more light on the morphology of HCN and the formation mechanism, the effects of the MCA amount and N_2 flow rate during annealing process were investigated. As shown in Fig.S4(see the Electronic Supplementary Material of this paper), hollow rods with large wall thickness and smooth surface were formed when the amount of MCA was 0.5 g and N_2 flow rate was 30 min/L[Fig.S4(A)]. No product was found in the magnetic boat when the amount of MCA was below 0.2 g owing to the complete pyrolysis. Regarding the influence of N_2 flow rate in the HCN formation, it was noticed that a flow of 20 mL/min leads to a mixture of hollow and solid rods, as for annealing 0.3 g of MCA[Fig.S4(B)]. Further increase in N_2 flow rate to 50 mL/min causes the damage of the tube structure of MCA and the formation of irregular blocks[Fig.S4(C)]. These blocks may be attributed to the lack of NH_3 and CO_2 gases, since they were rapidly removed by the high N_2 flow. In the light of these results, we inferred that as the MCA precursors were heated in the magnetic boat covered with tin foil, owing to a defect density existed at the center of the MCA crystal[19,31,36], the triazine molecules in the inner part of rods may quick sublime to produce NH_3 and CO_2 during thermal polycondensation, leading to the rods gradually extended outward to form hollow structures. These released gases were drew away with the N_2 flow, acting as etching agent to generate holes on the rods surface, as indicated by the SEM and TEM images of HCN obtained by annealing 0.3 g of MCA under N_2 with a flow rate of 30 mL/min. These holes in turn could ensure

the gases diffusion. As the thickness of the layer made of 0.5 g of MCA evenly spread in the magnetic boat become thicker, the resistance to gases diffusion increased. As the N_2 flow rate decreased to 20 mL/min, lower amount of NH_3 and CO_2 was drawn away by N_2 flow. Both of them suppressed the diffusion of NH_3 and CO_2, leading to thermal condensation of the MCA into g-C_3N_4 rods without holes on the surface.

The specific surface area and pore volume of the HCN and BCN were assessed by N_2 adsorption-desorption at 77 K (Fig.3). Both samples exhibited type IV isotherms with an H3-type hysteresis loop, indicating the presence of mesopores and macropores[33]. HCN has higher specific surface area(89.4 m^2/g) compared to BCN sample(6.02 m^2/g). The BJH pore size distribution curves displayed in Fig.3(B) confirm the presence of mesopores of various sizes for HCN, being consistent with SEM and TEM observations.

XRD patterns of NiMo cocatalyst and NiMo/HCN photocatalysts are depicted in Fig.2. The main diffraction peaks of cocatalyst are ascribed to MoO_2(JCPDS No. 76-1807) and metallic Ni(JCPDS No. 04-0850) crystalline phases. SEM and STEM-EDX images[Fig.1(C) and Fig.S5, see the Electronic Supplementary Material of this paper] reveal that NiMo cocatalyst displays a spherical morphology. For the synthesized NiMo/HCN photocatalysts, the characteristic diffraction peaks of g-C_3N_4(27.0°) and Ni(44.4°) are displayed in the corresponding XRD patterns. In addition, representative SEM image of 1% NiMo/HCN sample[Fig.1(D)] shows fewer particles attached on the surface of HCN. The results are further confirmed by the TEM images for HCN and 1% NiMo/HCN (Fig.4). As observed, many mesopores and macropores with sizes ranging from 20 nm to 150 nm exist on the surface of HCN. Some black spots of various sizes are observed on the surface of HCN, which are NiMo NPs[Fig.4(B)]. In the HRTEM image [Fig.4(C)], lattice fringes with interlayer distances of 0.20 and 0.24 nm are observed and assigned to (111) and (111) planes, respectively, of Ni and MoO_2.

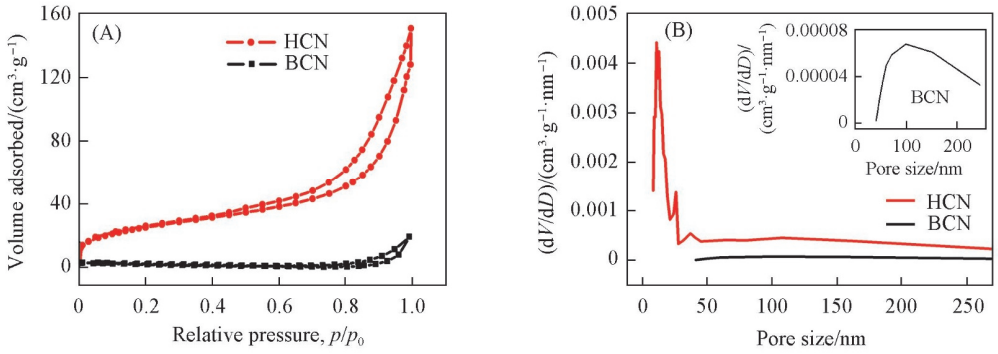

Fig.3 N_2 adsorption-desorption isotherms(A) and pore size distribution curves(B) of HCN and BCN

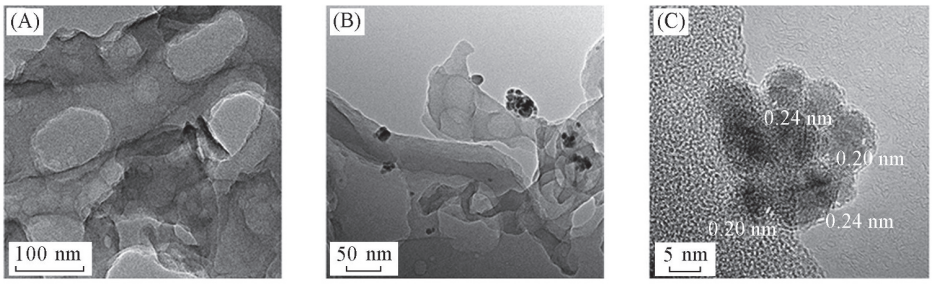

Fig.4 TEM images of HCN(A) and 1% NiMo/HCN(B), and HRTEM image of 1% NiMo/HCN(C)

Fig.5 shows the high-resolution XPS spectra of corresponding elements in 1% NiMo/HCN. The high-resolution C_{1s} spectrum[Fig.5(A)] displays binding energies(BEs) at 284.8, 288.2, and 293.8 eV, which belong to adventitious hydrocarbons on the edges of heptazine units, N—C=N, and C satellite peak, respectively[32,37]. The peaks located at 398.6, 399.2, 400.5, and 404.7 eV in the N_{1s} spectrum[Fig.5(B)] correspond to C—N=C, N—$(C)_3$, C—N—H, and π excitations of C=N conjugated structures in CN[38]. The Mo_{3d} spectrum[Fig.5(C)] displays two weak peaks at 229.4 and 231.9 eV, which can be assigned to Mo(IV) $3d_{5/2}$ and Mo(IV) $3d_{3/2}$, respectively. Meanwhile, the BEs originated from Mo(VI)(235.0 eV) was also observed owing to the surface oxidation of Mo(VI) in air[39,40]. In the Ni_{2p} spectrum, the characteristic peak of metallic Ni at 852.1 eV was found, and the other peaks were originated from the oxidized Ni species and satellite peaks [Fig.5(D)]. In the O_{1s} spectrum, the peaks at 530.9, 531.7, and 532.3 eV[Fig.5(E)] can be assigned to the lattice oxygen O^{2-}, surface-adsorbed oxygen and adsorbed molecular water, respectively.

To assess the light harvesting capacity of the prepared samples, UV-Vis DR spectra of samples were recorded(Fig.6). The HCN exhibits stronger light absorption in 420—650 nm compared to BCN[Fig.3(B)]. The band gaps of the HCN and BCN were estimated to be 2.67 and 2.62 eV, respectively (Fig.S6, see the Electronic Supplementary Material of this paper). After decorating HCN with NiMo, the obtained photocatalysts show enhanced absorption in the range of 450—800 nm. Furthermore, a red shift of absorption edge and an increase in absorption intensity in 450—800 nm with increasing NiMo loading amount were observed.

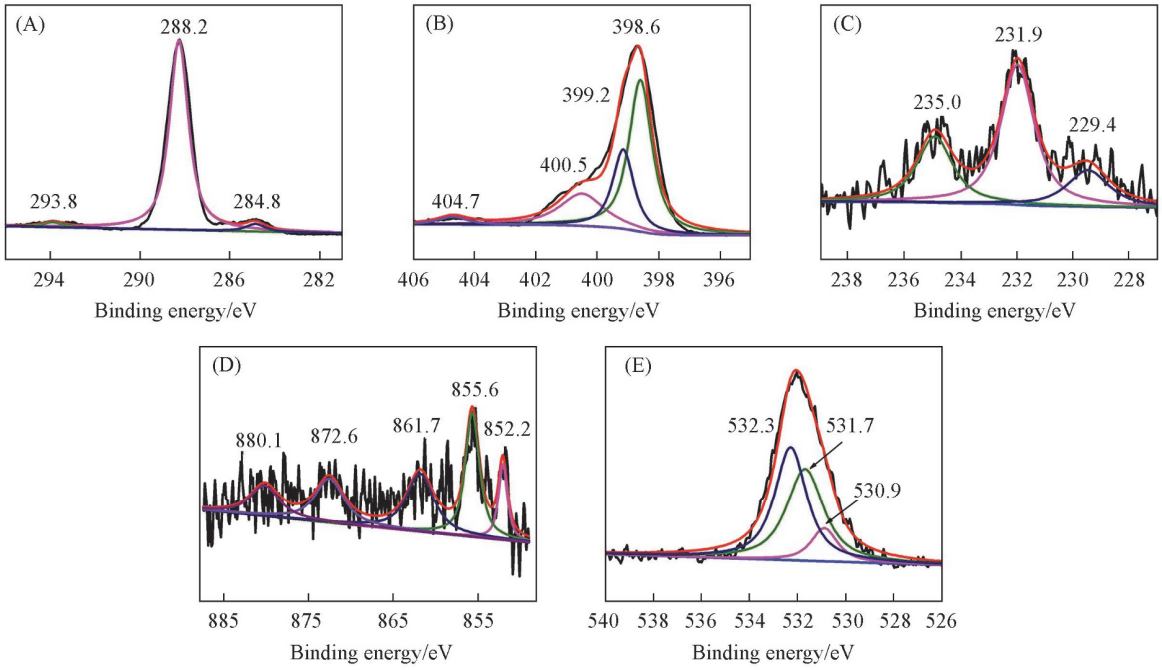

Fig.5 High-resolution XPS spectra of C_{1s}(A), N_{1s}(B), Mo_{3d}(C), Ni_{2p}(D) and O_{1s}(E) in 1% NiMo/HCN photocatalyst

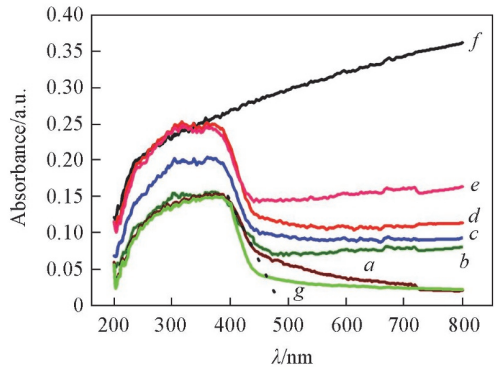

Fig.6 UV-Vis DR spectra of HCN(*a*), NiMo/HCN loading with 0.5%(*b*), 1%(*c*), 2%(*d*), and 3% NiMo(*e*), NiMo(*f*) and BCN(*g*)

The separation of photogenerated electron-hole pairs in NiMo/HCN and HCN was evaluated based on the PL[Fig.7(A)] and photocurrent[Fig.7(B)] spectra. The intensity of PL was reduced while the photocurrent was largely improved after decoration HCN with 1% NiMo, indicating the positive role of NiMo on the charge separation of HCN. Moreover, the charge-transfer resistance over 1% NiMo/HCN significantly decreased compared to HCN, indicating that decorating HCN with NiMo can facilitate the charge separation and retard their recombination.

3.2 Photocatalytic Production of H_2 and H_2O_2

Fig.8(A) shows the photocatalytic H_2 evolution activity of the obtained samples. No detectable H_2 amount was evolved in the presence of BCN or HCN. After loading 0.5% NiMo on HCN, the photocatalyst exhibits a rate of 3.34 μmol/h for H_2 production. An optimal rate of 8.08 μmol/h and an AQE of 4.98% were obtained for 1% NiMo-modified HCN. Control experiments demonstrated that no H_2 was evolved over 1% NiMo-decorated BCN, primarily because of the large particle size (Fig.S7, see the Electronic Supplementary Material of this paper) and the low S_{BET}(6.02 m^2/g) of BCN. Furthermore, HCN and BCN with 1.0% loading of Pt also exhibited relatively low H_2 evolution rates of *ca.* 4.69 and 1.03 μmol/h, respectively, indicating that a cost-effective NiMo loaded on HCN is an excellent cocatalyst for enhancing the photocatalytic H_2 evolution, as compared to 1% Pt/HCN. Compared to 1% Pt/BCN and 1% NiMo/BCN photocatalysts, the higher photocatalytic

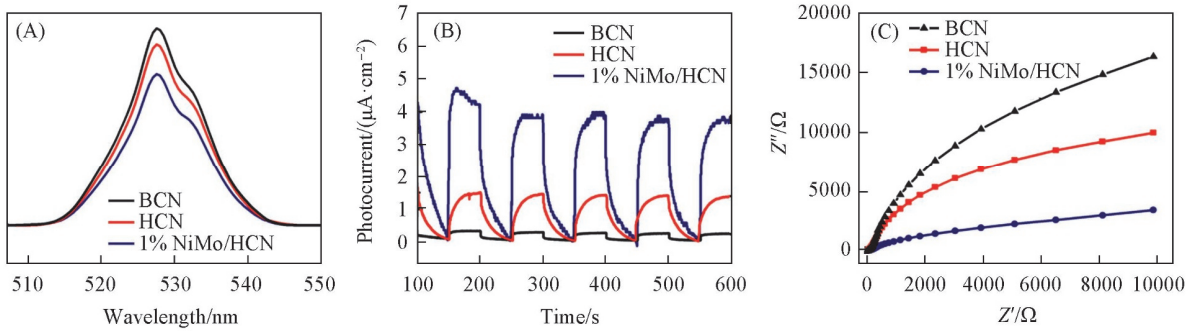

Fig.7 PL spectra(A), transient photocurrent responses(B), and EIS(C) of BCN, HCN and 1% NiMo/HCN

activity of the NiMo- and Pt-modified HCN is due to the relatively larger specific surface area and porous structures of HCN that facilitate the transfer of charge carriers(Fig.7). Further increase NiMo loading to 2%(4.21 μmol/h) and 3%(2.69 μmol/h) has no positive effect on increasing the H_2 production activity. Fig.8(B) shows the stability of H_2 evolution over 1% NiMo/HCN. The system was evacuated every 3 h and the process was carried out for five consecutive cycles. A slight decrease in H_2 evolution activity was noticed after five cycles. The XRD patterns of the used and fresh 1% NiMo/HCN catalysts are similar(Fig.S8, see the Electronic Supplementary Material of this paper), indicating its good stability for H_2 production in 15% TEOA aqueous solution.

The photocatalytic activity of BCN, HCN, 1% NiMo-modifed BCN and HCN in the reduction of O_2 to produce H_2O_2 in the presence of 5% ethanol solution was also evaluated [Fig.9(A)]. No H_2O_2 can be detected in the absence of photocatalyst. The H_2O_2 production activity over 1% NiMo/HCN is around 6.13 μmol/h, which is about 1.6 and 1.8 times higher than that of HCN(3.53 μmol/L) and 1% NiMo/BCN(3.43 μmol/L). The recyclability tests of the catalyst revealed that the amount of produced H_2O_2 was still high(15.45 μmol) after three consecutive cycles within 180 min of irradiation, as shown in Fig.9(B).

During photocatalytic H_2O_2 production, the decomposition of H_2O_2 also proceeds($H_2O_2+H^++e^-\longrightarrow H_2O+OH^\bullet$) as a result of the accumulation of electrons[41]. Thus, the photocatalytic decomposition of H_2O_2 was also discussed herein and the results are depicted in Fig.9(C). For BCN as catalyst, 67.4% of H_2O_2 was decomposed within 3 h. The H_2O_2 decomposition decreased to 43.3% over HCN and to 34.9% over 1% NiMo/HCN, indicating that the porous structure of HCN alongside the presence of NiMo cocatalyst improved electrons-holes separation efficiency. The results further indicated that the suppression of H_2O_2 decomposition over the 1% NiMo/HCN enhances the yield of H_2O_2 production.

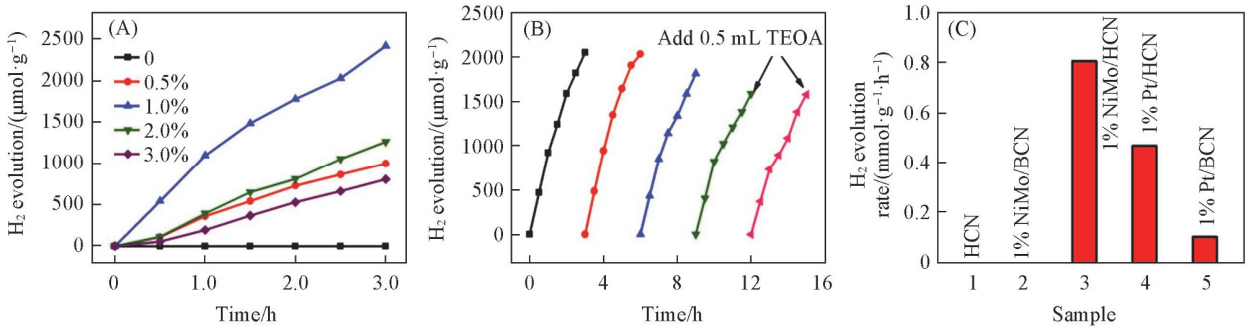

Fig.8 H_2 production over HCN and NiMo/HCN with various NiMo loadings(A), H_2 production for five consecutive catalytic cycles over 1% NiMo/HCN photocatalyst(B), and H_2 production rate over various photocatalysts(C)

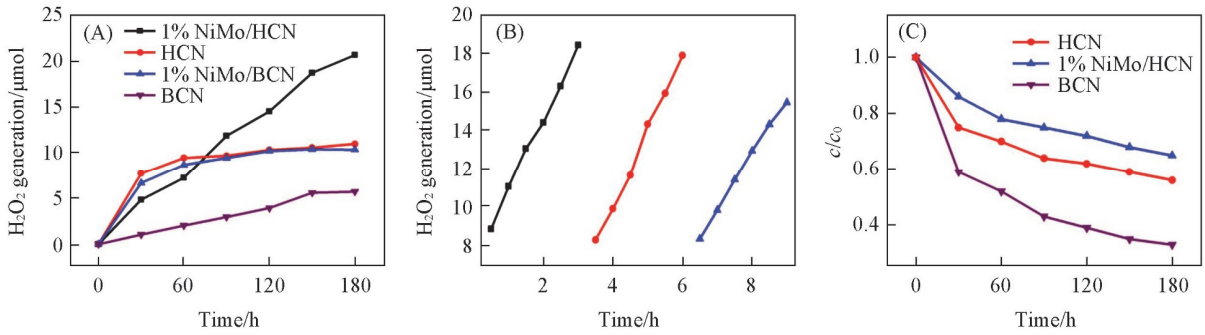

Fig.9 H_2O_2 production over HCN, 1% NiMo/HCN, BCN, and 1% NiMo/BCN(A), H_2O_2 production for three consecutive experiments over 1% NiMo/HCN photocatalyst(B), and photocatalytic decomposition of H_2O_2(1 mmol/L) under visible light irradiation(C)

Fig.10 illustrates the ESR spectra of DMPO-$^\bullet O^{2-}$ adduct for HCN and 1% NiMo/HCN. The characteristic signals of DMPO-$^\bullet O^{2-}$ are clearly observed, indicating that $^\bullet O^{2-}$ is the intermediate in the H_2O_2 production. Moreover, the signal of DMPO-$^\bullet O^{2-}$ adduct for 1% NiMo/HCN was much stronger than that for HCN, which proved the effective charge carries separation in NiMo-modified HCN. Control experiments confirmed that no H_2O_2 can be detected over 1% NiMo/HCN under dark or when the O_2 was replaced by N_2. These results suggested that the H_2O_2 is mainly produced from the reduction of O_2 by the photogenerated electrons[42,43]. The H_2O_2 production activity decreased to 1.35 μmol/L over 1% NiMo/HCN in ultrapure water, suggesting that the process of water oxidation by photogenerated holes has no contribution to H_2O_2 production.

According to our previously reported results[44], Ni has the electron conduction ability, while MoO_2 has the electron storage ability. In line with these results, we hypothesize that the bicomponent NiMo cocatalyst also has the ability of trapping electrons due to Ni and accepting electrons from g-C_3N_4 due to MoO_2 for an effective electron-hole separation and fast electron transfer. Thus, a possible mechanism of

photocatalytic production of H_2 and H_2O_2 over NiMo/HCN is proposed and illustrated in Scheme 2. HCN absorbed solar light and generated electrons and holes. The electrons from HCN can be transferred to MoO_2 "vessel" due to its large specific capacitance[44], and then transferred to Ni, thus inhibited the combination of the photogenerated charge carriers in HCN. The electrons gathered in Ni reacted with H^+ to produce H_2 molecules[Scheme 2(A)], or reacted with O_2 to produce $^{\bullet}O_2^-$ and then H_2O_2 molecules[Scheme 2(B)]. In summary, the large specific surface area and abundant active sites of HCN and the synergy between MoO_2 and Ni account for the greatly improved the photocatalytic H_2 and H_2O_2 production activity of NiMo/HCN.

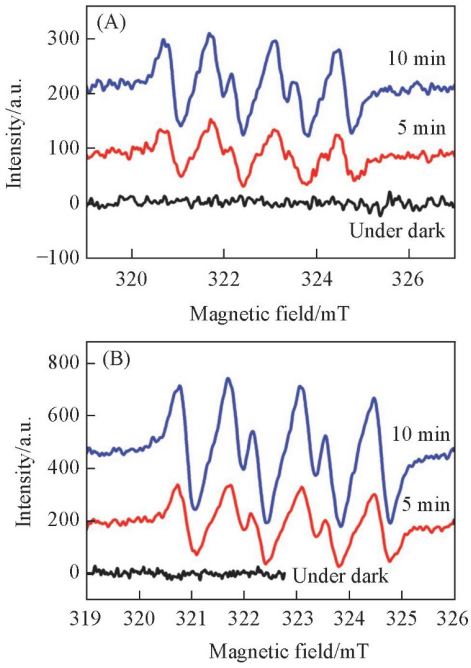

Fig.10 ESR spectra of DMPO-$^{\bullet}O^{2-}$ in the suspension of HCN(A) and 1% NiMo/HCN(B)

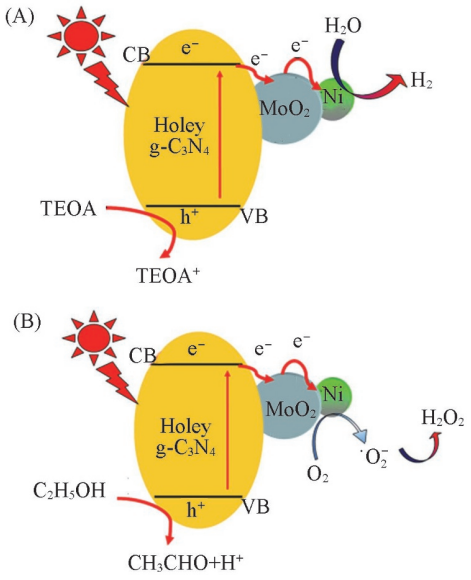

Scheme 2 Proposed photocatalytic mechanisms for H_2(A) and H_2O_2(B) production over NiMo/HCN photocatalyst under light irradiation

4 Conclusions

In this work, HCN was successfully prepared by the simple one-step thermal polymerization of MCA precursor obtained by hydrothermal treatment of melamine at 190 °C. A new bicomponent NiMo NPs cocatalyst was obtained by $NaBH_4$ reduction process and used to decorate HCN, aiming to develop an efficient photocatalyst for H_2 production from water reduction and H_2O_2 production from photo-reduction of O_2. The H_2 evolution rate over the optimum catalyst(1% NiMo/HCN) is 8.08 μmol/h compared to no activity over HCN and 1% NiMo/BCN and 4.69 μmol/h over 1% Pt/HCN. Meanwhile, the H_2O_2 production activity over 1% NiMo/HCN is 6.13 μmol/h, which is higher than that of HCN(3.53 μmol/L). Such an enhancement was explained by (i) the large surface area of HCN and unique holes on its surface, which provided abundant active sites for proton and O_2 reduction and charge carriers transfer, (ii) synergy between MoO_2 and Ni, which acted as a reservoir to store electrons from HCN and as actives sites for proton and O_2 reduction, respectively. Our findings could provide a new method for the design of HCN to expand its photocatalytic application fields.

Electronic Supplementary Material

Supplementary material is available in the online version of this article at http://dx.doi.org/10.1007/s40242-020-0067-5.

References

[1] Wang Z., Li C., Domen K., *Chem. Soc. Rev.*, **2019**, *48*(7), 2109
[2] Xu C., Anusuyadevi P. R., Aymonier C., Luque R., Marre S., *Chem. Soc. Rev.*, **2019**, *48*(14), 3868
[3] Ong W. J., Tan L. L., Ng Y. H., Yong S. T., Chai S. P., *Chem. Rev.*, **2016**, *116*(12), 7159
[4] Wen J. Q., Xie J., Chen X. B., Li X., *Appl. Sur. Sci.*, **2017**, *391*, 72
[5] Cao S., Low J., Yu J., Jaroniec M., *Adv. Mater.*, **2015**, *27*(13), 2150
[6] Zhang S., Gu P. C., Ma R., Luo C. T., Wen T., Zhao G. X., Cheng W. C., Wang X. K., *Catal. Today*, **2019**, *335*, 65
[7] Mishra A., Mehta A., Basu S., Shetti N. P., Reddy K. R., Aminabhavi T. M., *Carbon*, **2019**, *149*, 693
[8] Shen R. C., Xie J., Xiang Q. J., Chen X. B., Jiang J. Z., Li X., *Chinese. J. Catal.*, **2019**, *40*, 240
[9] Ren D., Zhang W., Ding Y., Shen R., Jiang Z., Lu X., Li X., *Solar RRL*, **2019**, 1900423
[10] Zhang G. G., Lan Z. A., Wang X. C., *Chem. Sci.*, **2017**, *8*(8), 5261
[11] Tian N., Huang H. W., Du X., Dong F., Zhang Y. H., *J. Mater. Chem. A*, **2019**, *7*(19), 11584
[12] Huang Z. W., Zhang Y., Dai H. Y., Wang Y. Y., Qin C. C., Chen W. X., Zhou Y. M., Yuan S. H., *J. Catal.*, **2019**, *378*, 331
[13] Wang T., Meng X., Li P., Ouyang S., Chang K., Liu G., Mei Z., Ye J., *Nano Energy*, **2014**, *9*, 50
[14] Huang Z. F., Song J., Pan L., Wang Z., Zhang X., Zou J. J., Mi W., Zhang X., Wang L., *Nano Energy*, **2015**, *12*, 646
[15] Liang Q. H., Li Z., Huang Z. H., Kang F. Y., Yang Q. H., *Adv. Func. Mater.*, **2015**, *25*(44), 6885
[16] Li Y. F., Jin R. X., Xing Y., Li J. Q., Song S. Y., Liu X. C., Li M., Jin R. C., *Adv. Energy Mater.*, **2016**, *6*(24), 1601273
[17] Zhou Y., Lv W. H., Zhu B. L., Tong F. J., Pan J., Bai J. R., Zhou Q. F.,

Qin H. F., *ACS Sustainable Chem. Eng.*, **2019**, *7*(6), 5801

[18] Huang H. W., Xiao K., Tian N., Dong F., Zhang T. R., Du X., Zhang Y., *J. Mater. Chem. A*, **2017**, *5*(33), 17452

[19] Guo S. E., Deng Z. P., Li M. X., Jiang B. J., Tian C. G., Pan Q. J., Fu H. G., *Angew. Chem. Int. Ed.*, **2016**, *55*(5), 1830

[20] Ai M. H., Zhang J. W., Gao R. J., Pan L., Zhang X. W., Zou J. J., *Appl. Catal. B: Environ.*, **2019**, *256*, 117805

[21] Ran J. R., Ma T. Y., Gao G., Du X. W., Qiao S. Z., *Energy Environ. Sci.,* **2015**, *8*(12), 3708

[22] Han Q., Wang B., Gao J., Cheng Z. H., Zhao Y., Zhang Z. P., Qu L.T., *ACS Nano*, **2016**, *10*(2), 2745

[23] Zhang Y. F., Park S. J., *J. Catal.*, **2019**, *379*, 154

[24] Ou H. H., Tang C., Zhang Y. F., Asiri A. M., Titirici M. M., Wang X. C., *J. Catal.*, **2019**, *375*, 104

[25] Yang P., Zhao J., Qiao W., Li L., Zhu Z., *Nanoscale*, **2015**, *7*(45), 18887

[26] Guo Q. Y., Zhang Y. H., Zhang H. S., Liu Y. J., Zhao Y. J., Qiu J., Dong G., *Adv. Funct. Mater.*, **2017**, *27*(42), 1703711

[27] Iqbal W., Dong C., Xing M., Tan X., Zhang J., *Catal. Sci. Technol.*, **2017**, *7*(8), 1726

[28] Cui Y., Zhang G., Lin Z., Wang X., *Appl. Catal. B: Environ.*, **2016**, *181*, 413

[29] Song X. P., Yang Q., Jiang X. H., Yin M. Y., Zhou L. M., *Appl. Catal. B: Environ.*, **2017**, *217*, 322

[30] Chen X. J., Shi R., Chen Q., Zhang Z. Y., Jiang W. J., Zhu Y. F., Zhang T. R., *Nano Energy*, **2019**, *59*, 644

[31] Zhou C., Shi R., Shang L., Wu L. Z., Tung C. H., Zhang T. R., *Nano Research*, **2018**, *11*(6), 3462

[32] Wang X. S., Zhou C., Shi R., Liu Q. Q., Waterhouse G. I., Wu L. Z., Tung C. H., Zhang T. R., *Nano Research*, **2019**, *12*(9), 2385

[33] Zhou B. X., Ding S. S., Zhang B. J., Xu L., Chen R. S., Luo L., Huang W. Q., Xie Z., Pan A., Huang G. F., *Appl. Catal. B: Environ.*, **2019**, *254*, 321

[34] Zhou L., Feng J. R., Qiu B. C., Zhou Y., Lei J. Y., Xing M. Y., Wang L., Zhou Y. B., Liu Y. D., Zhang J. L., *Appl. Catal. B: Environ.*, **2020**, *267*, 118396

[35] Xu J. X., Qi Y. H., Wang C., Wang L., *Appl. Catal. B: Environ.*, **2019**, *241*, 178

[36] Li J. E., Wang Y. W., Xu W. N., Wang Y., Zhang B., Luo S., Zhou X. Y., Zhang C. L., Gu X., Hu C. G., *Nano Energy*, **2019**, *57*, 379

[37] Jun Y. S., Lee E. Z., Wang X. C., Hong W. H., Stucky G. D., Thomas A., *Adv. Funct. Mater.*, **2013**, *23*(29), 3661

[38] Shalom M., Inal S., Fettkenhauer C., Neher D., Antonietti M., *J. Am. Chem. Soc.*, **2013**, *135*(19), 7118

[39] Wang X., Ma Z. J., Chai L. L., Xu L. Q., Zhu Z. Y., Hu Y., Qian J. J., Huang S. M., *Carbon*, **2019**, *141*, 643

[40] Han X., Xu D. Y., An L., Hou C. Y., Li Y., Zhang Q. H., Wang H. Z., *Appl. Catal. B: Environ.*, **2019**, *243*, 136

[41] Tsukamoto D., Shiro A., Shiraishi Y., Sugano Y., Ichikawa S., Tanaka S., Hirai T., *ACS Catal.*, **2012**, *2*(4), 599

[42] Yang Y., Zeng Z. T., Zeng G., Huang D. L., Xiao R., Zhang C., Zhou C. Y., Xiong W. P., Wang W. J., Cheng M. J., *Appl. Catal. B: Environ.*, **2019**, *258*, 117956

[43] Zheng Y., Yu Z., Ou H., Asiri A. M., Chen Y., Wang X., *Adv. Funct. Mater.*, **2018**, *28*(10), 1705407

[44] Xu J. X., Ji Q. J., Yan X. M., Wang C., Wang L., *Appl. Catal. B: Environ.*, **2020**, *268*, 118739